Progress In Electromagnetics Research C, Vol. 96, 165–177, 2019

Application of Symplectic MRTD with CPML in Analysis of EMP Propagation in Tunnel

Guohui Li[1] and Yawen Liu[2, *]

Abstract—In this paper, the implementation of convolution perfectly matched layer (CPML) with good absorbing property is proposed for the symplectic multi-resolution time-domain (SMRTD) method, and a side-wall vault-top tunnel model is established by using the equidistant equation. The radian of the tunnel can be selected in the range of 0–$\pi/2$ according to actual needs. The absorbing performances of perfect matched layer (PML) and CPML are compared in the proposed tunnel model. In addition, based on the straight tunnel model and curved tunnel model with different radians, the characteristic of field cross-section distribution of electromagnetic pulse (EMP) propagation excited by TE_{10} mode is studied.

1. INTRODUCTION

Finite-difference time-domain (FDTD) [1–4] method has become a common method for electromagnetic numerical calculation because of its simplicity and intuition. The FDTD method can directly solve the Maxwell curl equation which depends on time, and it is easy to deal with the case of inhomogeneous media by approximating the time and space differential operators in the curl equation with the second-order accuracy of central difference. However, its calculation accuracy is relatively low, and the time step of calculation is also relatively low. The size of time steps and spatial discrete grids must satisfy the Courant-Friedrichs-Levy (CFL) stability condition, and the error will accumulate with the increase of calculation time. To overcome these shortcomings of FDTD method, paper [5] proposed MRTD method to improve the calculation accuracy, but MRTD method requires more stability conditions; Chen and Zhang [6] proposed ADl-MRTD to get rid of CFL stability conditions. However, the numerical dispersion of ADl-MRTD method is worse than that of FDTD method. In a word, the effect of these methods is not satisfactory because they destroy the structure of Maxwell equation. Because Maxwell equation can be regarded as an infinite dimensional Hamilton system, and the evolution of the system over time is always symplectic transformation,the correct discrete algorithm should be symplectic transformation, which is called Hamilton algorithm or symplectic algorithm [7–12].

In order to keep the internal structure of Maxwell equation in discrete solution, Wei et al. [13] rewrote Maxwell equation into Hamilton equation. In time domain, symplectic propagator technique was used to discretize the equation; in space domain, time domain multi-resolution method was used to discrete the Maxwell equation; and symplectic algorithm for solving Maxwell equation, namely symplectic time domain multi-resolution (S-MRTD) method, was constructed. The stability and numerical dispersion of S-MRTD method are systematically discussed. It is reported that the stability and numerical dispersion of S-MRTD method are better than FDTD and MRTD, that is, with the same calculation conditions, the calculation accuracy of S-MRTD method is higher.

Received 7 August 2019, Accepted 9 October 2019, Scheduled 26 October 2019

* Corresponding author: Yawen Liu (liuyawen1111@163.com).

[1] College of Mathematics and Information Science, Weifang University, Weifang 261061, China. [2] Army Engineering University of PLA, Nanjing 210007, China.

In this work, the CFS-PML based on a stretched-coordinate and a recursive convolution is developed for the S-MRTD scheme. This method referred here is called convolution perfectly matched layer (CPML) [14, 15]. It is shown that the implementation of CPML is independent of the material medium, that is no matter in homogeneous, inhomogeneous, lossy, dispersive, anisotropic, or nonlinear media, the implementation can be used without any modification. In addition, due to the actual needs, the study of the propagation characteristics of non-nuclear electromagnetic pulse in tunnels has attracted the attention of many scholars, and the interest stems from two application areas: electromagnetic protection against the EMP weapons, which are mainly of interest for the military applications and the ultra-wideband (UWB) communication in tunnel driven by the commercial application. Predominating the characteristic of the field cross-section distribution of the EMP propagation in tunnel, we could install the sensitive electromagnetic devices or the shielding equipments such as wave-guide widows, metallic doors, and filters at the place where the filed distribution is weak, or change the distributed direction of some components to weaken the coupling energy. For the wireless communication, we could install the antennae at the place where the field distribution is strong to get high coupling energy. In this paper, we have established a model of side-wall arch-top tunnel. The radian of the model can be chosen arbitrarily in the range of 0–$\pi/2$ according to actual needs. In order to compare the absorbing performance of Berenger's PML [16] and CPML in this tunnel model, we design a calculation example, and the numerical results show that the CPML has a better absorbing performance. In order to study the distribution of cross-sectional field intensity of non-nuclear electromagnetic pulses in tunnels, the S-MRTD method with CPML absorbing boundary condition (ABC) is introduced into the tunnel model. By analyzing the characteristics of field cross-section distribution of non-nuclear electromagnetic pulse in straight and curved tunnels, some useful conclusions are obtained.

2. APPLICATION OF CPML TO SMRTD METHOD

When simulating electromagnetic wave propagation, it is usually necessary to truncate the analysis area somewhere outside the physical region, which usually results in the reflection of the wave back to the region of interest, and the non-physical wave reflection may interact with the incident physical wave. To avoid this problem, we can specify an appropriate set of differential equations on the truncated boundary, or add a layer capable of absorbing the propagation waves. In this work, we use the method of adding a perfect matching layer (PML) to the downstream and forward positions of the truncated boundary.

Following the work in [16], the Maxwell's equations (MEs) are first rewritten to their equivalent time harmonic equations. In addition to introducing the stretched coordinate metrics into MEs, the recursive convolution method originally proposed in [17] is used to accelerate the convolution operator. Then the modified MEs in the frequency domain can be transformed back to the time domain equation by Fourier transform. And the MEs in CPML can then be derived.

In the CPML layer, the formula is posed in the stretched coordinate space. Without losing generality, we assume a lossy medium here. Therefore, the x-projection of Ampere's law is specified as

$$j\omega\varepsilon E_x + \sigma E_x = \frac{1}{s_y}\frac{\partial}{\partial y}H_z - \frac{1}{s_z}\frac{\partial}{\partial z}H_y \tag{1}$$

where s_i is the stretched-coordinate metric and defined as

$$s_i = \kappa_i + \frac{\sigma_i}{\alpha_i + j\omega\varepsilon_0}, \quad i = x, y, z \tag{2}$$

where $\alpha_i > 0, \sigma_i > 0, \kappa_i \geq 1$.

Defining that $s_i' = s_i^{-1}$, we can get:

$$s_i' = \frac{1}{\kappa_i} + \frac{\sigma_i'}{\alpha_i' + j\omega\varepsilon_i'}, \tag{3}$$

where $\sigma_i' = -\sigma_i$, $\varepsilon_i' = \varepsilon_0\kappa_i^2$ and $\alpha_i' = \kappa_i^2\alpha_i + \kappa_i\sigma_i$. Using Laplace transform theory, it can be shown that s_i' has the impulse response

$$s_i'(t) = \frac{\delta(t)}{\kappa_i} + \frac{\sigma_i'}{\varepsilon_i'}e^{-\frac{\alpha_i'}{\varepsilon_i'}t}u(t) = \frac{\delta(t)}{\kappa_i} + \zeta_i(t) \tag{4}$$

where $\delta(t)$ is the unit impulse function, and $u(t)$ is the step function. Inserting Eq. (4) into Eq. (1), then transform Eq. (1) into time domain:

$$\begin{aligned}\varepsilon_r\varepsilon_0\frac{\partial E_x(t)}{\partial t}+\sigma E_x(t) &= s_y'(t)*\frac{\partial}{\partial y}H_z(t)-s_z'(t)*\frac{\partial}{\partial z}H_y(t)=\frac{1}{\kappa_y}\frac{\partial}{\partial y}H_z(t)-\frac{1}{\kappa_z}\frac{\partial}{\partial z}H_y(t)\\ &+\int_0^t\frac{\partial}{\partial y}H_z(t-\tau)\,\zeta_y(\tau)\,d\tau-\int_0^t\frac{\partial}{\partial z}H_y(t-\tau)\,\zeta_z(\tau)\,d\tau \end{aligned} \tag{5}$$

The field dispersion in space domain for symplectic MRTD method is consistent with that in MRTD method. As for time discretization, unlike MRTD method, the symplectic MRTD method combines time components and coefficients to form a new function, so for simplicity, the E_x field component is expanded in terms of Daubechies scaling functions in space domain

$$E_x(\mathbf{r},t)=\sum_{i,\,j=-\infty}^{+\infty}E^{\phi x}_{i+1/2,\,j,\,k}(t)\phi_{i+1/2}(x)\,\phi_j(y)\,\phi_k(z) \tag{6}$$

where $E^{\phi x}_{i+1/2,\,j,\,k}$ is the coefficient for the field in terms of scaling functions which is equal to the corresponding field. Indices i, j, and k are the discrete space indices related to the space coordinates via $x=i\Delta x$, $y=j\Delta y$ and $z=k\Delta z$, where Δx, Δy, and Δz represent the space discretization intervals in x-, y-, and z-directions. Function $\phi(v)$ is defined as Daubechies' scaling function.

With the wavelet-Galerkin scheme based on Daubechies' compactly supported wavelets, the following equations can be obtained

$$\begin{aligned}&\varepsilon_r\varepsilon_0\frac{\partial E^{\phi x}_{i+\frac{1}{2},\,j,\,k}(t)}{\partial t}+\sigma E^{\phi x}_{i+\frac{1}{2},\,j,\,k}(t)\\ =\;&\frac{1}{\kappa_y\Delta y}\sum_l a(l)H^{\phi z}_{i+\frac{1}{2},\,j+l+\frac{1}{2},\,k}(t)-\frac{1}{\kappa_z\Delta z}\sum_l a(l)H^{\phi y}_{i+\frac{1}{2},\,j,\,k+l+\frac{1}{2}}(t)\\ &+\frac{1}{\Delta y}\int_0^t\sum_l a(l)H^{\phi z}_{i+\frac{1}{2},\,j+l+\frac{1}{2},\,k}(t-\tau)\,\zeta_y(\tau)\,d\tau-\frac{1}{\Delta z}\int_0^t\sum_l a(l)H^{\phi y}_{i+\frac{1}{2},\,j,\,k+l+\frac{1}{2}}(t-\tau)\,\zeta_x(\tau)\,d\tau\end{aligned} \tag{7}$$

where coefficients $a(l)$ for $0\le l\le 2$ have been tabulated in [18]. Defining that

$$\psi_{e_{xy},\,i+1/2,\,j,\,k}(t)=\frac{1}{\Delta y}\int_0^t\sum_l a(l)H^{\phi z}_{i+\frac{1}{2},\,j+l+\frac{1}{2},\,k}(t-\tau)\,\zeta_y(\tau)\,d\tau \tag{8}$$

$$\psi_{e_{xz},\,i+1/2,\,j,\,k}(t)=\frac{1}{\Delta z}\int_0^t\sum_l a(l)H^{\phi y}_{i+\frac{1}{2},\,j,\,k+l+\frac{1}{2}}(t-\tau)\,\zeta_x(\tau)\,d\tau \tag{9}$$

After the time domain is discretized by 5-stage and 4-order explicit symplectic integral, the following iteration equation can be obtained from Eq. (7)

$$\begin{aligned}E^{\phi x,\,n+v/m}_{i+1/2,\,j,\,k} &= CA_{i+1/2,\,j,\,k}E^{\phi x,\,n+(v-1)/m}_{i+1/2,\,j,\,k}+CB_{i+1/2,\,j,\,k}\left[\left(\frac{1}{\kappa_y\Delta y}\sum_l a(l)H^{\phi z,n+v/m}_{i+1/2,\,j+l+1/2,\,k}\right.\right.\\ &\left.\left.-\frac{1}{\kappa_z\Delta z}\sum_l a(l)H^{\phi y,\,n+v/m}_{i+1/2,\,j,\,k+l+1/2}\right)+\psi^{n+v/m}_{e_{xy},\,i+1/2,\,j,\,k}-\psi^{n+v/m}_{e_{xz},\,i+1/2,\,j,\,k}\right]\end{aligned} \tag{10}$$

where

$$\psi^{n+v/m}_{e_{xy},\,i+1/2,\,j,\,k}=b_y\psi^{n+(v-1)/m}_{e_{xy},\,i+1/2,\,j,\,k}+\frac{a_y}{\Delta y}\sum_l a(l)H^{\phi z,\,n+v/m}_{i+1/2,\,j+l+1/2,\,k} \tag{11}$$

$$\psi^{n+v/m}_{e_{xz},\,i+1/2,\,j,\,k}=b_z\psi^{n+(v-1)/m}_{e_{xz},\,i+1/2,\,j,\,k}+\frac{a_z}{\Delta z}\sum_l a(l)H^{\phi y,\,n+v/m}_{i,\,j+l+1/2} \tag{12}$$

$$a_i=\frac{\sigma_i}{\sigma_i\kappa_i+\kappa_i^2\alpha_i}\left(e^{-\left(\frac{\sigma_i}{\kappa_i}+\alpha_i\right)\frac{d_v\Delta t}{\varepsilon_0}}-1\right),\quad b_i=e^{-\left(\frac{\sigma_i}{\kappa_i}+\alpha_i\right)\frac{d_v\Delta t}{\varepsilon_0}},\quad i=y,z \tag{13}$$

$$CA_{i+1/2,\,j,\,k} = \frac{2\varepsilon_{i+1/2,\,j,\,k} - \sigma_{i+1/2,\,j,\,k} d_v \Delta t}{2\varepsilon_{i+1/2,\,j,\,k} + \sigma_{i+1/2,\,j,\,k} d_v \Delta t} \tag{14}$$

$$CB_{i+1/2,\,j,\,k} = \frac{2 d_v \Delta t}{2\varepsilon_{i+1/2,\,j,\,k} + \sigma_{i+1/2,\,j,\,k} d_v \Delta t} \tag{15}$$

Similarly, the other Ampere's and Faraday's equations in the convolution perfect matching absorbing layers are as follows

$$\begin{aligned} E^{\phi x,\,n+v/m}_{i+1/2,\,j,\,k} &= CA_{i+1/2,\,j,\,k} E^{\phi x,\,n+(v-1)/m}_{i+1/2,\,j,\,k} + CB_{i+1/2,\,j,\,k} \left[\left(\frac{1}{\kappa_y \Delta y} \sum_l a(l) H^{\phi z,\,n+v/m}_{i+1/2,j+l+1/2,\,k} \right.\right. \\ &\left.\left. - \frac{1}{\kappa_z \Delta z} \sum_l a(l) H^{\phi y,\,n+v/m}_{i+1/2,\,j,\,k+l+1/2} \right) + \psi^{n+v/m}_{e_{xy},\,i+1/2,\,j,\,k} - \psi^{n+v/m}_{e_{xz},\,i+1/2,\,j,\,k} \right] \end{aligned} \tag{16}$$

$$\begin{aligned} E^{\phi y,\,n+v/m}_{i,\,j+1/2,\,k} &= CA_{i,\,j+1/2,\,k} E^{\phi y,\,n+(v-1)/m}_{i,j+1/2,\,k} + CB_{i,\,j+1/2,\,k} \left[\frac{1}{\kappa_z \Delta z} \sum_l a\,(l) H^{\phi x,\,n+v/m}_{i,\,j+1/2,\,k+l+1/2} \right. \\ &\left. - \frac{1}{\kappa_x \Delta x} \sum_l a\,(l) H^{\phi z,\,n+v/m}_{i+1/2,\,j+l+1/2,\,k} + \psi^{\phi y,n+v/m}_{e_{yz},\,i,\,j+1/2,k} - \psi^{\phi y,\,n+v/m}_{e_{yx},\,i,\,j+1/2,\,k} \right] \end{aligned} \tag{17}$$

$$\begin{aligned} E^{\phi z,\,n+v/m}_{i,\,j,\,k+1/2} &= CA_{i,\,j,\,k+1/2} E^{\phi z,\,n+(v-1)/m}_{i,\,j,\,k+1/2} + CB_{i,\,j,\,k+1/2} \left[\frac{1}{\kappa_x \Delta x} \sum_l a\,(l) H^{\phi y,\,n+v/m}_{i+l+1/2,\,j,\,k+1/2} \right. \\ &\left. - \frac{1}{\kappa_y \Delta y} \sum_l a\,(l) H^{\phi x,\,n+v/m}_{i,\,j+l+1/2,\,k+1/2} \right] + CB_{i,\,j,\,k+\frac{1}{2}} \left(\psi^{\phi z,n+v/m}_{e_{zx},\,i,\,j,\,k+1/2} - \psi^{\phi z,\,n+v/m}_{e_{zy},\,i,\,j,\,k+1/2} \right) \end{aligned} \tag{18}$$

$$\begin{aligned} H^{\phi x,\,n+v/m}_{i,\,j+1/2,k+1/2} &= CP_{i,j+1/2,\,k+1/2} H^{\phi x,n+(v-1)/m}_{i,\,j+1/2,\,k+1/2} \\ &- CQ_{i,\,j+1/2,k+1/2} \left[\frac{1}{\kappa_y \Delta y} \sum_l a\,(l) E^{\phi z,\,n+(v-1)/m}_{i,\,j+l+1,\,k+1/2} - \frac{1}{\kappa_z \Delta z} \sum_l a\,(l) E^{\phi y,\,n+(v-1)/m}_{i,\,j+1/2,\,k+l+1} \right] \\ &- CQ_{i,\,j+1/2,k+1/2} \left(\psi^{n+(v-1)/m}_{h_{xy} i,\,j+1/2,k+1/2} - \psi^{n+(v-1)/m}_{h_{xz} i,\,j+1/2,k+1/2} \right) \end{aligned} \tag{19}$$

$$\begin{aligned} H^{\phi y,\,n+v/m}_{i+1/2,\,j,\,k+1/2} &= CP_{i+1/2,j,k+1/2} H^{\phi y,n+(v-1)/m}_{i+1/2,\,j,\,k+1/2} \\ &- CP_{i+1/2,\,j,\,k+1/2} \left[\frac{1}{\kappa_z \Delta z} \sum_l a\,(l) E^{\phi x,\,n+(v-1)/m}_{i+1/2,\,j,\,k+l+1} - \frac{1}{\kappa_x \Delta x} \sum_l a\,(l) E^{\phi z,\,n+(v-1)/m}_{i+l+1,\,j,\,k+1/2} \right] \\ &- CP_{i+1/2,\,j,\,k+1/2} \left(\psi^{n+(v-1)/m}_{h_{yz} i+1/2,\,j,\,k+1/2} - \psi^{n+(v-1)/m}_{h_{yx} i+1/2,\,j,\,k+1/2} \right) \end{aligned} \tag{20}$$

$$\begin{aligned} H^{\phi z,\,n+v/m}_{i+1/2,\,j+1/2,\,k} &= CQ_{i+1/2,\,j+1/2,\,k} H^{\phi z,\,n+(v-1)/m}_{i+1/2,\,j+1/2,\,k} \\ &- CP_{i+1/2,\,j+1/2,k} \left[\frac{1}{\kappa_x \Delta x} \sum_l a\,(l) E^{\phi y,\,n+(v-1)/m}_{i+l+1,\,j+1/2,\,k} - \frac{1}{\kappa_y \Delta y} \sum_l a\,(l) E^{\phi x,\,n+(v-1)/m}_{i+1/2,\,j+l+1,\,k} \right] \\ &- CP_{i+1/2,\,j+1/2,\,k} \left(\psi^{n+(v-1)/m}_{h_{zx} i+1/2,\,j+1/2,\,k} - \psi^{n+(v-1)/m}_{h_{zy} i+1/2,\,j+1/2,\,k} \right) \end{aligned} \tag{21}$$

where c_v and d_v are the symplectic integrator propagator time coefficients with the following values [13]

$$\begin{aligned} c_1 &= c_5 = 0.17399689, \quad c_2 = c_4 = -0.12038504, \quad c_3 = 0.89277630, \\ d_1 &= d_4 = 0.62337932, \quad d_2 = d_3 = -0.12337932, \quad d_5 = 0. \end{aligned}$$

3. ESTABLISHMENT OF THE TUNNEL MODEL

The model established in this paper is a vault tunnel model, which consists of three parts, two of which are straight tunnel, and one of which is arc tunnel. Fig. 1–Fig. 3 show the tunnel's 3D model, each component and section, respectively. The corresponding radian of the arc tunnel is α, and the angle between the two straight tunnels is π-α. The cross-section perpendicular to the direction of the tunnel is a side-wall vault. As shown in Fig. 3(b), the vault is semi-circular, and the cross-section size along the direction of the tunnel is equal everywhere. Each of the three curves in Fig. 3(a) consists of two straight lines and an arc line. The left one is the projection of the left wall on the ground, which is defined as Γ_1; the middle one is the central curve along the direction of the tunnel, which is defined as Γ_0; and the right one is the projection of the right wall on the ground, which is defined as Γ_2. Since the cross-sections perpendicular to the direction of the tunnel are equal, the curves on the left and right sides must be equidistant from the center line, and the distance between them is $rr = (R - r)/2$. According to the equidistant equation, the equation of left and right curves can be derived from the equation of central line, which are the projections of left and right side walls on the ground, so that the position of side walls can be determined.

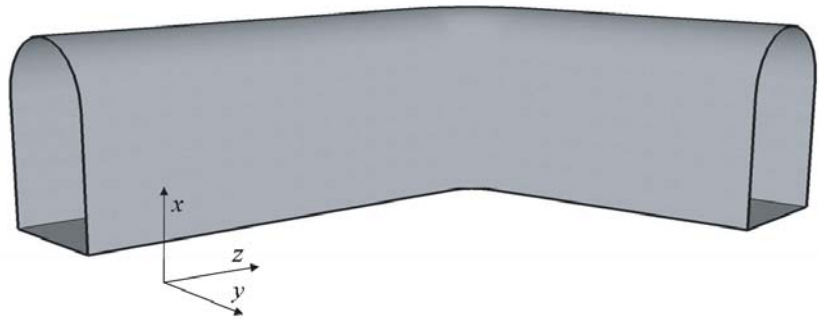

Figure 1. Three-dimensional model of the vault tunnel.

Figure 2. Components of the vault tunnel.

From Fig. 3, the center line equation can be obtained as follows

$$\Gamma_0 \begin{cases} y = y_1 + rr & (z_1 \le z \le z_2) \\ y = y_o - \sqrt{r_m^2 - (z - z_2)^2} & (z_2 < z \le z_m) \\ y = y_m + (z - z_m)\tan\alpha & (z_m < z \le z_{me}) \end{cases} \tag{22}$$

The equidistant equation can be shown as

$$\Gamma_{1,2} \begin{cases} Y = y \mp \dfrac{a}{\sqrt{1 + y'^2}} \\ Z = z \pm \dfrac{ay'}{\sqrt{1 + y'^2}} \end{cases} \quad (0 < a) \tag{23}$$

Here Eq. (23) is a parametric equation with z as its parameter, in which a denotes the distance of any point on the central curve Γ_0 moving in both positive and negative directions along the normal of

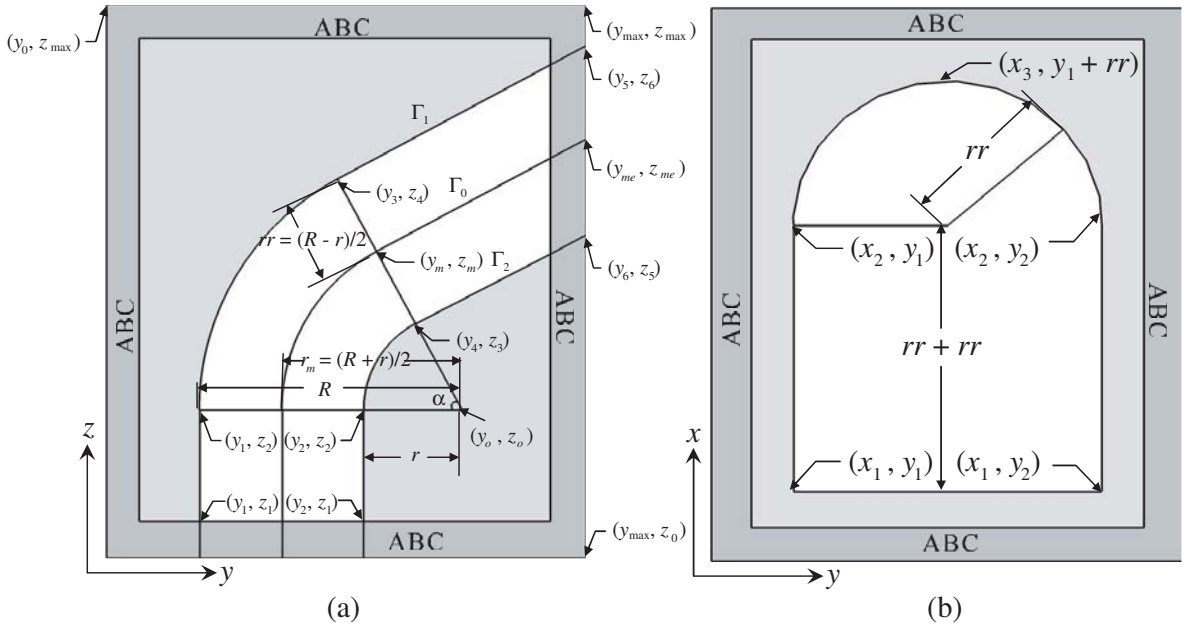

Figure 3. Profiles of the vault tunnel model. (a) Profile at $x = x_2$. (b) Profile at $z = z_2$.

the point. From Eq. (22), the equations of Γ_1 and Γ_2 can be obtained as follows

$$\Gamma_1 \begin{cases} y = y_1 & (z_1 \le z \le z_2) \\ y = y_o - \sqrt{R^2 - (z - z_2)^2} & (z_2 < z \le z_4) \\ y = y_3 + (z - z_4)\tan\alpha & (z_4 < z \le z_6) \end{cases} \tag{24}$$

$$\Gamma_2 \begin{cases} y = y_2 & (z_1 \le z \le z_2) \\ y = y_o - \sqrt{r^2 - (z - z_2)^2} & (z_2 < z \le z_3) \\ y = y_4 + (z - z_3)\tan\alpha & (z_3 < z \le z_5) \end{cases} \tag{25}$$

Since the side walls are perpendicular to the ground, Eqs. (24) and (25) are also the surface equations of the side walls.

As shown Fig. 4, if we use a plane parallel to the ground to intercept the vault, we can get two intersecting lines Γ_3 and Γ_4 on both sides of the vault. Since all cross-sections along the tunnel are equal, the two intersections are similar to those of Γ_1 and Γ_2, and are equidistant from the center line Γ_0. However, the distances from the center line are different, and they vary with the height x. The line spacing can be calculated from Fig. 3(a). Defining that the line spacing is r_x, we can get

$$r_x = \sqrt{rr^2 - (x - x_2)^2} \tag{26}$$

Define that the left intersection line is Γ_3, and the right intersection line is Γ_4. Similar to the derivation of Eq. (24) and Eq. (25), the equation of Γ_3 and Γ_4 can be obtained as follows

$$\Gamma_3 \begin{cases} y = y_1 + rr - r_x & (z_1 \le z \le z_2) \\ y = y_o - \sqrt{(R - r_x)^2 - (z - z_2)^2} & (z_2 < z \le z_m + r_x \sin\alpha) \\ y = y_m - r_x\cos\alpha + (z - z_m - r_x\sin\alpha)\tan\alpha & (z_m + r_x\sin\alpha < z \le z_m + r_x\sin\alpha + \\ & (y_{\max} - R + r_x\cos\alpha)\cot\alpha) \end{cases} \tag{27}$$

$$\Gamma_4 \begin{cases} y = y_1 + rr + r_x & (z_1 \le z \le z_2) \\ y = y_o - \sqrt{(r + r_x)^2 - (z - z_2)^2} & (z_2 < z \le z_m - r_x \sin\alpha) \\ y = y_m + r_x\cos\alpha + (z - z_m + r_x\sin\alpha)\tan\alpha & (z_m - r_x\sin\alpha < z \le z_m - r_x\sin\alpha + \\ & (y_{\max} - r - r_x\cos\alpha)\cot\alpha) \end{cases} \tag{28}$$

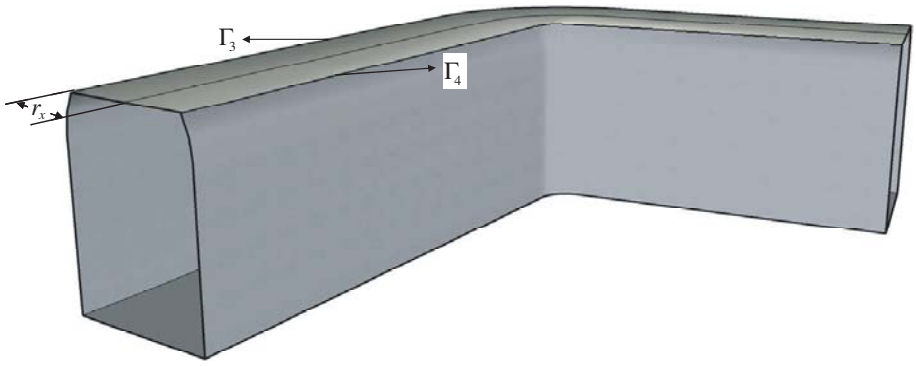

Figure 4. Diagram of equidistant line at the tunnel vault.

Γ_3 and Γ_4 represent any two intersecting lines at different x coordinates, so Γ_3 is the left side surface equation of the vault, and Γ_4 is the right side surface equation of the vault. So far, the mathematical model of the tunnel has been established completely. The constitutive parameters for the wall and edge of the bending part can be defined via conformal technique [19], and the conformed sections of the tunnel are shown as in Fig. 5.

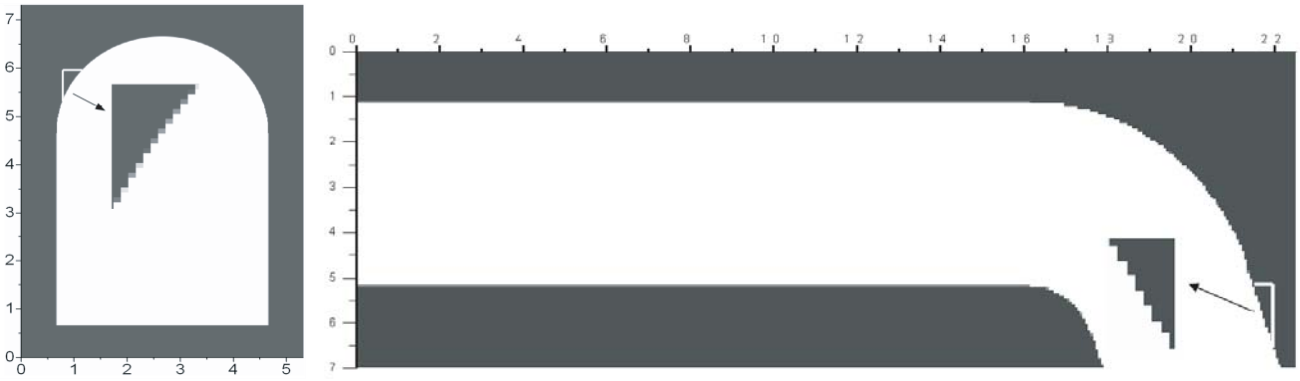

Figure 5. The conformed sections of the vault and bending part of the tunnel.

4. PERFORMANCE COMPARISON AND ANALYSIS OF ABSORBING BOUNDARY CONDITIONS

In this section, the proposed computational model is used to verify the absorption performance of the PML and CPML. In the example, the calculation model is set up as shown in Fig. 6. The length of the straight tunnel, the length of the bottom, and the height of the side wall are all 2.0 m; the radius of the vault is 1.0 m; and the radian of the bend is $\pi/2$. The space steps and time steps of the computational domain are chosen as $\Delta x = \Delta y = \Delta z = \delta = 0.02\,\text{m}$ and $\Delta t = \delta/3c$, where c is the velocity of light in vacuum. The computational region except the boundary layer contains $180 \times 153 \times 253$ cells, which are truncated by 8-layer PML and CPML absorbing boundary conditions, respectively. In order to investigate the reflection error, a reference space is set up, which expands 100 space steps in all directions on the basis of the original computational space. The results obtained are taken as reference results.

Gauss pulse is chosen as the time function of the forced excitation source, whose expression is as follows

$$g(t) = 10^4 \exp\left(-4\pi\left(\frac{t-t_0}{\tau}\right)^2\right) \tag{29}$$

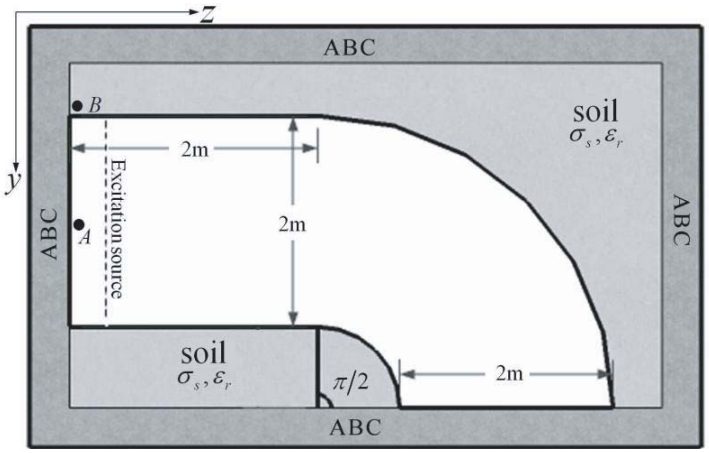

Figure 6. Computational model of the tunnel.

where $t_0 = 1.5 \times 10^{-9}$, $\tau = 2 \times 10^{-9}$. Here, TE_{10} and TM_{11} propagation modes are introduced into the computational model as forced excitation sources, respectively. Suppose that the section width of the tunnel is a and that the height is b, then the TE_{10} propagation mode is defined as

$$\left.\begin{aligned} E_y &= -\frac{j\omega\mu a}{\pi} A \sin\left(\frac{\pi}{a}x\right) e^{-j\beta_{10}z} \\ H_x &= \frac{j\beta_{10} a}{\pi} A \sin\left(\frac{\pi}{a}x\right) e^{-j\beta_{10}z} \\ H_z &= A \cos\left(\frac{\pi}{a}x\right) e^{-j\beta_{10}z} \\ E_x &= E_z = H_y = 0 \end{aligned}\right\} \tag{30}$$

And the TM_{11} propagation model is defined as

$$\left.\begin{aligned} E_x &= -\frac{j\beta_{11}}{k_c^2}\frac{\pi}{a} A \cos\left(\tfrac{\pi}{a}x\right) \sin\left(\frac{\pi}{b}y\right) e^{-j\beta_{11}z} \\ E_y &= -\frac{j\beta_{11}}{k_c^2}\frac{\pi}{b} A \sin\left(\tfrac{\pi}{a}x\right) \cos\left(\frac{\pi}{b}y\right) e^{-j\beta_{11}z} \\ E_z &= A \sin\left(\frac{\pi}{a}x\right) \sin\left(\frac{\pi}{b}y\right) e^{-j\beta_{11}z} \\ H_x &= \frac{j\omega\varepsilon}{k_c^2}\frac{\pi}{b} A \sin\left(\frac{\pi}{a}x\right) \cos\left(\frac{\pi}{b}y\right) e^{-j\beta_{11}z} \\ H_y &= -\frac{j\omega\varepsilon}{k_c^2}\frac{\pi}{a} A \cos\left(\frac{\pi}{a}x\right) \sin\left(\frac{\pi}{b}y\right) e^{-j\beta_{11}z} \\ H_z &= 0 \end{aligned}\right\} \tag{31}$$

As shown in Fig. 6, we select a reference point A with coordinates (85, 18, 9), and the reflection error is defined as

$$\text{error}_{\text{dB}} = 20 \log_{10} \frac{\left|\chi_i(t) - \chi_{i_{ref}}(t)\right|}{\left|\chi_{i_{ref_{\max}}}(t)\right|} \tag{32}$$

where $\chi_i(t)$ represents E_y component of point A in the original calculation space; $\chi_{i_{ref}}(t)$ represents E_y component of point A in the reference space; and $\chi_{i_{ref_{\max}}}(t)$ represents the maximum value of $\chi_{i_{ref}}(t)$. Fig. 7 and Fig. 8 show the electric field reflection errors with the PML and CPML when TE_{10} mode and TM_{11} mode are introduced, respectively.

From Fig. 7 and Fig. 8, it can be seen that the reflection error in traditional PML lasts until the late stage of the pulse. This is because the low-frequency evanescent wave is the main factor

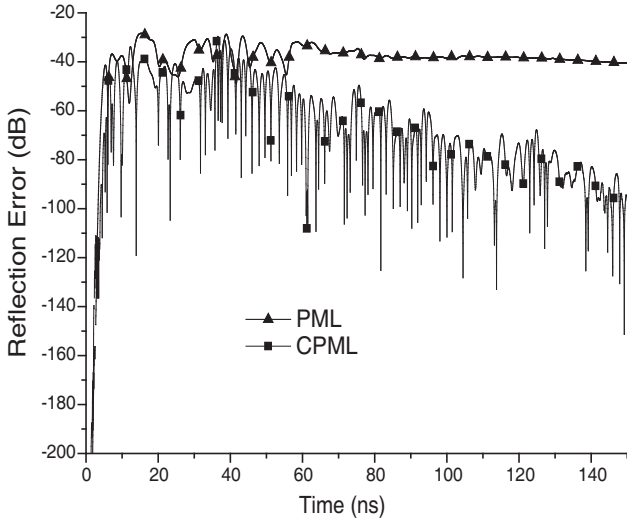

Figure 7. Reflection error (TE_{10}).

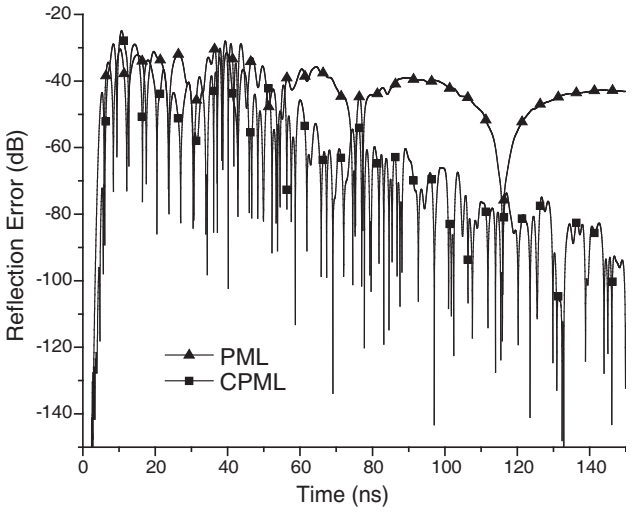

Figure 8. Reflection error (TM_{11}).

in the late stage of the pulse, while the absorption ability of traditional PML to the low-frequency evanescent wave is poor, which results in a large late reflection [20]. In contrast, CPML has shown great advantages in solving this problem. The CPML can effectively absorb low-frequency evanescent waves and overcome the late reflection caused by long-time calculation, thus ensuring the overall absorption performance of the absorbing boundary conditions. In addition, compared with the traditional PML, the implementation of CPML is independent of the nature of the media in the truncated region and suitable for dispersive media, anisotropic media, and nonlinear media. All we need is to modify the corresponding terms on the left side of Eq. (7), so CPML is simpler and more convenient to implement.

5. FIELD DISTRIBUTION ON CROSS-SECTION OF THE TUNNEL

5.1. Field Distribution on Cross-Section Excited by TE_{10} Mode in Straight Tunnel

The computational model in this section refers to Section 3. As a straight tunnel, $\alpha = 0$; the length of the bottom and the height of the side wall of the tunnel cross-section are defined as 4 m; and the radius of the vault is defined as 2 m. It is known that a tunnel with vault section is essentially a lossy waveguide. When the frequency is higher than the cutoff frequency, the wave can propagate along the tunnel axis. In the process of wave propagation, it is attenuated because part of the electromagnetic energy penetrates into the rock and soil medium. In this work, we use the field mode in the ideal waveguide to excite the tunnel, which results in that the cross-section distribution of the field near the excitation surface varies along the axis. The cross-sectional distribution of the field will be stable to the inherent field model of the tunnel through a long distance propagation. Fig. 9 shows the field distributions on the cross-section of the tunnel after the field distribution is stable. The UWB electromagnetic pulse is used as the time function of the excitation source, and the field value is normalized. It can be seen from the figure that the field distribution in the tunnel section is complex and far from that in the ideal waveguide, but some characteristics are similar to that in the ideal waveguide, and the field distribution is still regular.

It can be seen from Fig. 9 that when TE_{10} mode excitation is applied, the field components in the tunnel are still mainly E_y and H_x, while the other field components are smaller, which is similar to the field components in the ideal waveguide. E_y and H_x components are basically standing waveform along x-direction, which is similar to ideal waveguide. However, the distributions of E_y and H_x along y-direction are very different from that of an ideal waveguide. In an ideal rectangular waveguide, E_y and H_x are invariable along the y-direction while in the tunnel, and the variation of E_y and H_x along the y-direction is similar to that along the x-direction, which is basically a standing wave. Therefore, in the tunnel, the electromagnetic field is strong in the middle and weak around, and the energy mainly concentrates in the center of the tunnel.

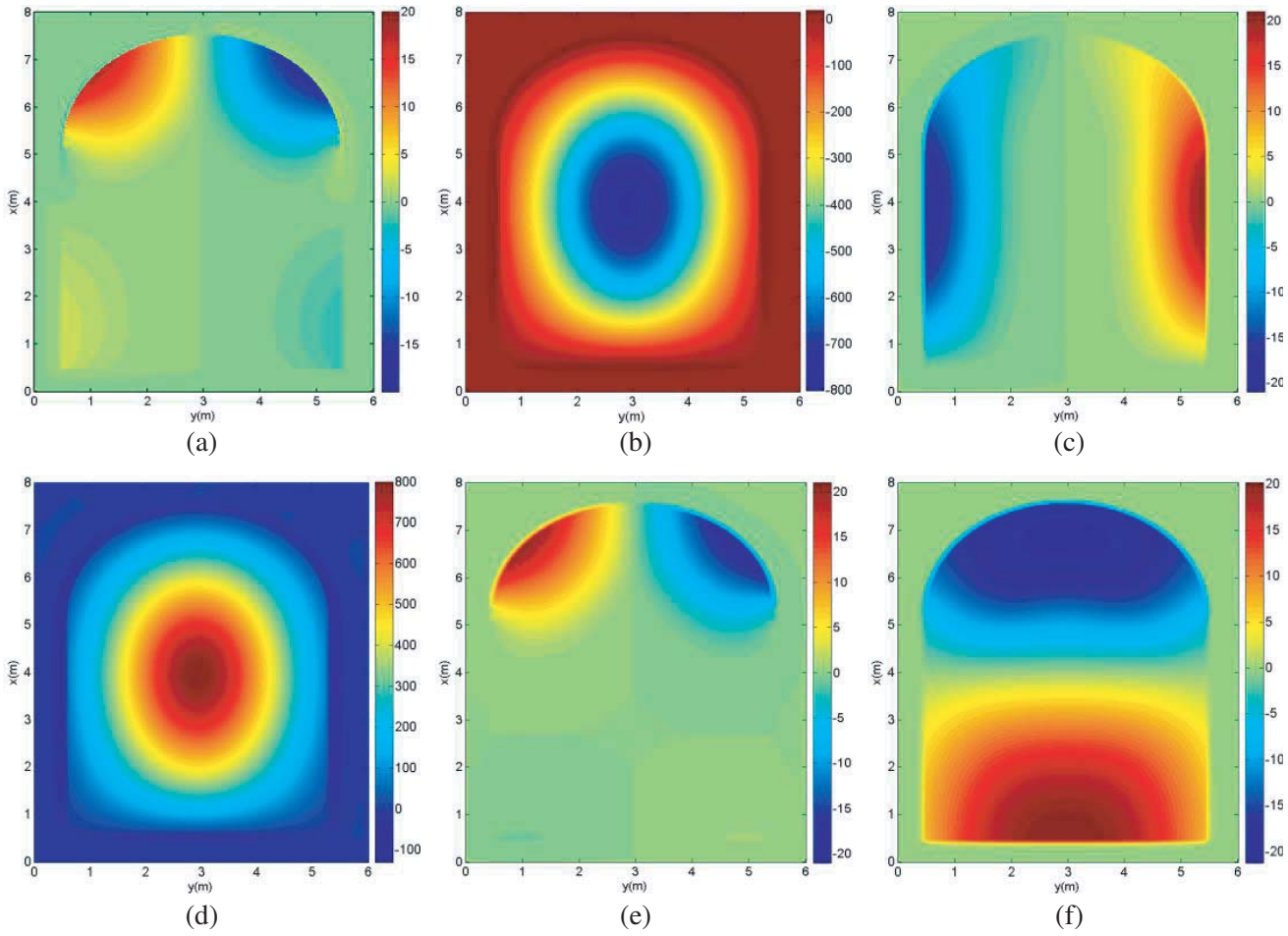

Figure 9. Cross-section field intensity distribution excited by TE_{10} mode. (a) Ex (V/m), (b) Ey (V/m), (c) Ez (V/m), (d) Hx (A/m), (e) Hy (A/m), (f) Hz (A/m).

E_x and H_y components are no longer zero as in ideal rectangular waveguide, but they are smaller except for the vault position. This is mainly because the boundary at the vault is not rectangular. Compared with an ideal waveguide, not only the dielectric parameters are different, but also the shape of the boundary changes abruptly.

The characteristic of H_z component in x-direction is similar to that in an ideal waveguide, that is, the field intensities at the top and bottom atre the largest, and the middle is smaller. The directions of field intensities at the top and bottom are opposite, and the characteristic of the field intensity along y-direction is very different from that in ideal waveguide and is no longer regular. In addition, the E_z component is no longer zero.

5.2. Field Distribution on Cross-Section Excited by TE_{10} Mode Near Bend

The calculation model used in this section refers to Section 3. In order to reflect the effect of bend on the cross-section field distribution, this section analyses the cross-section field distribution at a distance of 1.5 meters from the bend. $\alpha = \pi/18$, $5\pi/18$, $\pi/2$, respectively.

Taking the electric field as an example, Fig. 10–Fig. 12 show the cross-section field distribution after TE_{10} mode excitation has reached a stable propagation in tunnels with different radians, and the field values are normalized. It can be seen from the figure that with the increase of the curvature of the bend, the cross-section distribution of each field becomes more and more disorderly, and the components transmitted into the geotechnical medium become particularly obvious, especially the distribution of

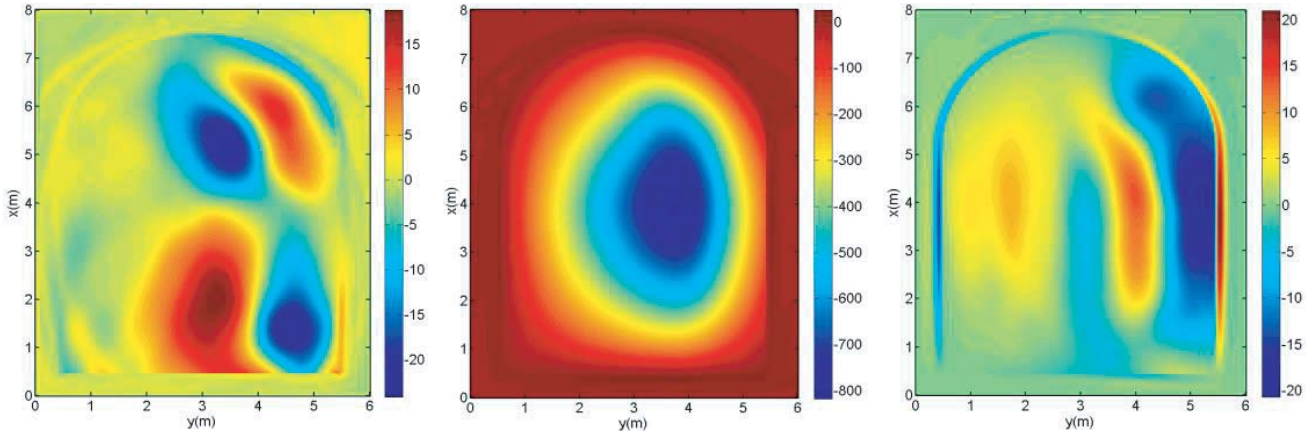

Figure 10. Cross-section field distribution excited by TE_{10} mode ($\alpha = \pi/18$). (a) Ex (V/m), (b) Ey (V/m), (c) Ez (V/m).

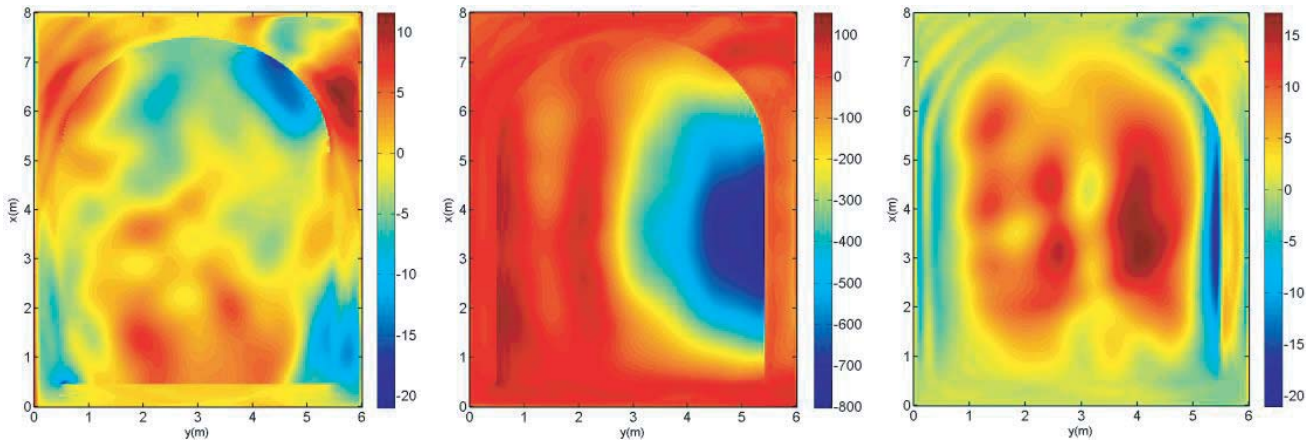

Figure 11. Cross-section field distribution excited by TE_{10} mode ($\alpha = 5\pi/18$). (a) Ex (V/m), (b) Ey (V/m), (c) Ez (V/m).

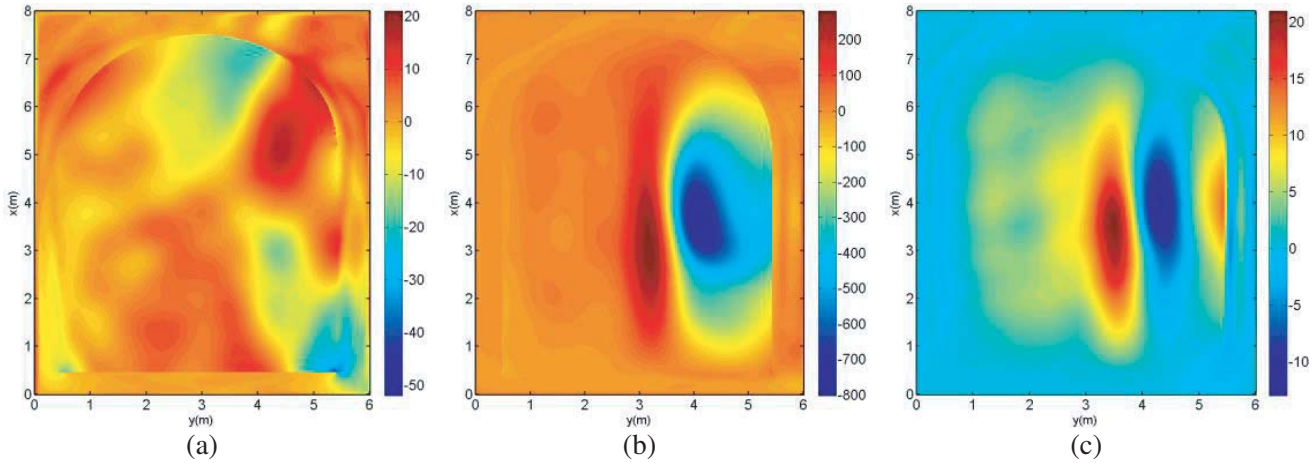

Figure 12. Cross-section field distribution excited by TE_{10} mode ($\alpha = \pi/2$). (a) Ex (V/m), (b) Ey (V/m), (c) Ez (V/m).

E_x component on the cross-section, which can even blurs the boundary between the tunnel and the geotechnical medium. However at the same time, we can see that the field intensity energy of each field quantity tends to concentrate on one side of the tunnel, and the direction of concentration is consistent with the direction of the tunnel bending, and the greater the curvature of the tunnel is, the more obvious the trend of concentration is.

6. CONCLUSION

In this paper, a novel implementation of CPML for SMRTD method has been introduced, and a side-wall vault-top tunnel model which can be selected in the range of 0–$\pi/2$ according to actual needs is established. The proposed tunnle model is used to verify the absorption performances of the PML and CPML. Numerical results show that the CPML can absorb low-frequency evanescent waves more effectively and overcome the late reflection caused by long-time calculation. In addition, we also analyze the characteristics of the cross-section field distribution in the tunnel excited by the TE_{10} mode. It is shown that in the straight tunnel, the cross-section distribution of each field component follows certain rules and has its own characteristics. Near the bend part of the tunnel, the energy of each field tends to concentrate on one side of the tunnel, and the direction of concentration is consistent with the direction of the bend of the tunnel. It is noted that the greater the curvature of the tunnel is, the more obvious the trend of concentration is.

ACKNOWLEDGMENT

The authors would like to thank the reviewers for helpful remarks.

REFERENCES

1. Taflove, A., *Computational Electrodynamics: The Finite-Difference Time-Domain Method*, Artech House, Norwood, MA, 2005.
2. Biswas, B., K. Ahmed, B. K. Paul, Md. A. Khalek, and M. S. Uddin, "Numerical evaluation of the performance of different materials in nonlinear optical applications," *Results in Physics*, Vol. 13, 102184, 2019.
3. Ahmed, K., B. K. Paul, Md. A. Jabin, and B. Biswas, "FEM analysis of birefringence, dispersion and nonlinearity of graphene coated photonic crystal fiber," *Ceramics International*, Vol. 45, 15343–15347, 2019.
4. Paul, B. K., K. Ahmed, S. A. M. Matiur Rahman, M. Shanthi, D. Vigneswaran, and R. Zakaria, "Numerical analysis of a highly nonlinear microstructured optical fiber with air-holes arranged in spirals," *Optical Fiber Technology*, Vol. 51, 90–95, 2019.
5. Krumpholz, M. and L. P. B. Katehi, "MRTD: New time-domain schemes based on multiresolution analysis," *IEEE Trans. Microwave Theory Tech.*, Vol. 44, 555–561, Apr. 1996.
6. Chen, Z. and J. Zhang, "An unconditionally stable 3-D ADI-MRTD method free of the CFL stability condition," *IEEE Microwave and Wireless Components Letters*, Vol. 11, 349–351, 2001.
7. Hirono, T., W. Lui, S. Seki, and Y. Yoshikuni, "A three-dimensional fourth-order finite-difference time-domain scheme using a symplectic integrator propagator," *IEEE Trans. Microwave Theory Tech.*, Vol. 49, 1640–1648, 2001.
8. Huang, Z., W. Sha, X. Wu, and M. Chen, "A novel high-order time-domain scheme for three-dimensional Maxwell's equations," *Microwave and Optical Technology Letters,* Vol. 48, 1123–1125, 2006.
9. Gao, Y. J., H. W. Yang, and G. B. Wang, "A research on the electromagnetic properties of plasma photonic crystal based on the symplectic finite-difference time-domain method," *Optik — International Journal for Light and Electron Optics,* Vol. 127, 1838–1841, 2016.

10. He, Z. F., S. Liu, S. Chen, and S. Y. Zhong, "Application of symplectic finite-difference time-domain scheme for anisotropic magnetised plasma," *IET Microwaves, Antennas & Propagation,* Vol. 11, 600–606, 2017.
11. Kuang, X., Z. Huang, M. Chen, and X. Wu, "High-order symplectic compact finite-different time-domain algorithm for guide-wave structures," *IEEE Microwave and Wireless Components Letters*, Vol. 29, 80–82, 2019.
12. Sha, W. E. I., X.-L. Wu, Z.-X. Huang, and M.-S. Chen, "Waveguide simulation using the high-order symplectic finite-difference time-domain scheme," *Progress In Electromagnetics Research B*, Vol. 13, 237–256, 2009.
13. Wei, M., Z. X. Huang, B. Wu, X. Wu, and H. Wang, "A novel symplectic multi-resolution time-domain scheme for electromagnetic simulations," *IEEE Microwave and Wireless Components Letters*, Vol. 23, 175–177, 2013.
14. Roden, J. and S. Gedney, "Convolution PML (CPML): An efficient FDTD implementation of the CFS-PML for arbitrary media," *Microwave and Optical Technology Letters,* Vol. 27, 334–339, 2000.
15. Liu, Y., P. Zhang, and Y.-W. Chen, "Implementation of the parallel higher-order FDTD with convolution PML," *Progress In Electromagnetics Research Letters,* Vol. 70, 129–138, 2017.
16. Berenger, J., "A perfectly matched layer for the absorption of electromagnetic waves," *Journal of Computational Physics*, Vol. 114, 185–200, 1994.
17. Luebbers, R., F. Huusberger, K. Kunz, R. Standler, and M. Schneider, "A frequency-dependent finite-difference time-domain formulation for dispersive materials," *IEEE Transactions on Electromagnetic Compatibility*, Vol. 32, 222–227, 1990.
18. Liu, Y., Y.-W. Chen, P. Zhang, and X. Xu, "Implementation and application of the spherical MRTD algorithm," *Progress In Electromagnetics Research*, Vol. 139, 577–597, 2013.
19. Yu, W. and R. Mittra, "A conformal finite difference time domain technique for modeling curved dielectric surfaces," *IEEE Microwave and Wireless Components Letters*, Vol. 11, 25–27, 2002.
20. Berenger, J., "An effective PML for the absorption of evanescent waves in waveguides," *IEEE Microwave and Guided Wave Letters*, Vol. 8, 188–190, 1998.